Journal of Zhejiang University-SCIENCE A (Applied Physics & Engineering)
ISSN 1673-565X (Print); ISSN 1862-1775 (Online)
www.zju.edu.cn/jzus; www.springerlink.com
E-mail: jzus@zju.edu.cn

Kinematic optimization of 2D plunging airfoil motion using the response surface methodology

Mahmoud MEKADEM[†1,3], Taha CHETTIBI[2], Samir HANCHI[1],
Laurent KEIRSBULCK[3], Larbi LABRAGA[3]

([1]*Fluids Mechanics Laboratory, Polytechnic Military School, Bordj el Bahri, Algiers 16045, Algeria*)
([2]*Structural Mechnics Laboratory, Polytechnic Military School, Bordj el Bahri, Algiers 16045, Algeria*)
([3]*TEMPO Laboratory, University of Valenciennes and Hainaut-Cambresis, 59313 Valenciennes Cedex 9, France*)
[†]E-mail: mahmoud.mekadem@univ-valenciennes.fr; mahmoud.mekadem@gmail.com

Received Dec. 11, 2010; Revision accepted Aug. 30, 2011; Crosschecked Dec. 14, 2011

Abstract: The propulsive efficiency of a plunging NACA0012 airfoil is maximized by means of a simple numerical optimization method based on the response surface methodology (RSM). The control parameters are the amplitude and the reduced frequency of the harmonic sinusoidal motion. The 2D unsteady laminar flow around the plunging airfoil is computed by solving the Navier-Stokes equations for three Reynolds number values ($Re = 3.3\times10^3$, 1.1×10^4, and 2.2×10^4). The Nelder-Mead algorithm is used to find the best control parameters leading to the optimal propulsive efficiency over the constructed response surfaces. It is found that, for a given efficiency level and regardless of the considered Re value, it is possible either to obtain high thrust by selecting a high oscillation frequency or to reduce the input power by adopting a low plunging amplitude.

Key words: Plunging airfoil, Propulsive efficiency, Optimization, Response surface methodology (RSM)
doi:10.1631/jzus.A1000502 **Document code:** A **CLC number:** TK83

1 Introduction

Fish swimming hydrodynamics has been the focus of researchers' interest for a long time. By observing the motion of aquatic species and evaluating their performance in various situations, scientists have concluded that fish and cetaceans employ their oscillating tail to produce both propulsive and maneuvering forces (Schouveiler *et al.*, 2005). Indeed, by tuning its own kinematics, a fish is able to swim efficiently and move silently with minimal wasted energy. This is accomplished by generating large thrust and turning forces.

Birds and insects have remarkable maneuvering capabilities. Bird flight is specifically characterized by low-frequency large-amplitude vertical oscillations. Insect flight is instead often described by high-frequency horizontal oscillations.

The understanding of these natural phenomena significantly contributes to the performance enhancement of air and/or water vehicles equipped with flapping wings, such as micro-air-vehicles (MAVs) and unmanned undersea vehicles (Shyy *et al.*, 1999).

The Reynolds number (Re) characterizing both MAV and insect flight ranges from 1×10^2 to 1×10^4, making flight control very difficult (Shyy *et al.*, 1999). Through observation, Knoller (1909) and Betz (1912) explained for the first time the mechanisms of propulsive force generation for flapping wings. They concluded that, during a flapping stroke, wings create both lift and thrust forces, via an induced effective angle of attack. Katzmayr (1922) conducted the first experimental work to verify the Knoller-Betz effect and confirmed the possibility of

thrust generation for the unsteadily moving wing.

Recent advances in the understanding of insect flight aerodynamics are mainly due to Dickinson and Götz (1993) and Dickinson *et al.* (1999). They highlighted the important contribution of the leading edge vortex appearance with stall delay (Dickinson and Götz, 1993; Ellington *et al.*, 1996). To explain the lift enhancement of flapping wings, several unsteady mechanisms have been proposed. These include the delayed stall, the Kramer effect (Ellington, 1984; Dickinson *et al.*, 1999), the added mass, and wake capture (Dickinson and Götz, 1993; Dickinson *et al.*, 1999). These distinct mechanisms were analyzed in depth by Sane (2003).

The flow around oscillating airfoils has been studied using experimental, computational, and analytical methods. Both the thrust generation mechanism and the propulsive efficiency optimization have been investigated. Garrick (1936) determined analytically the thrust force using Theodorsen's linearized solution for an incompressible unsteady flow around a harmonically oscillating flat plate (Theodorsen, 1935). For $Re = 4 \times 10^4$ and under optimal control parameters, Anderson *et al.* (1998) obtained experimentally a propulsive efficiency (ratio of output to input powers) of about 87%. In the case of combined plunging and pitching motions of an NACA0012 airfoil, they found that the efficiency peak occurs in the Strouhal number range of 0.25 to 0.40. Lai and Platzer (1999) performed flow visualizations and laser Doppler velocimeter (LDV) measurements in a water tunnel. They demonstrated that the wake pattern behind a plunging NACA0012 airfoil changes from a drag-indicative wake to a thrust-producing jet for a Strouhal number larger than 0.13. Moreover, they confirmed that the plunge velocity is an appropriate parameter to study the flow field in a plunging airfoil. Heathcote *et al.* (2008) performed an experimental study of the aerodynamic forces generated by a heaving NACA0012 hydrofoil for Re between 1×10^4 and 3×10^4. By introducing spanwise flexibility, they obtained a 50% thrust increase without increasing the input power. Jones and Platzer (1997; 2001) and Jones *et al.* (1998) performed experimental and numerical studies over a large range of control parameters and illustrated the power-extraction capabilities of various flapping foil mechanisms. These studies allowed the design of a successful flapping MAV prototype.

In the case of a single plunging airfoil, and for $Re = 3 \times 10^6$ and the Mach number $M = 0.3$, Tuncer and Platzer (2000) numerically obtained an optimal propulsive efficiency of about 70%. This value corresponds to low reduced frequencies and high plunge amplitudes. For a tandem configuration of flapping and stationary airfoils, they obtained an efficiency larger than 40%. They also found that, for low-frequency low-amplitude flapping motions, both the propulsive efficiency and the thrust are decreased by viscous and nonlinear effects. Isogai *et al.* (1999) corroborated this conclusion with a numerical calculation of the dynamic stall phenomenon around an oscillating airfoil and for various combinations of reduced frequency, phase angle, and amplitude. Ramamurti and Sandberg (2001) performed numerical simulations of the unsteady flow around an oscillating NACA0012 airfoil using a finite element incompressible Navier-Stokes solver at $Re = 1.1 \times 10^3$. They found that the maximum thrust is obtained when the phase angle between the pitching and the plunging motions is $\varphi = 120°$, and the maximum value of the propulsive efficiency η occurs at $\varphi = 90°$. Using a compressible 2D Navier-Stokes solver, Young and Lai (2004; 2007) performed both a flow field calculation and a wake structure visualization for a plunging NACA0012 airfoil at $Re = 2 \times 10^4$. They reported that the wake pattern and the aerodynamic forces developed by the airfoil are very sensitive to trailing-edge effects.

Various aspects of flapping flight and thrust generation mechanisms have been exhaustively reviewed by Shyy *et al.* (1999) and Platzer *et al.* (2008). A fundamental aspect arising from the aforementioned studies is that the propulsive efficiency η and the thrust coefficient C_t produced by flapping airfoils are antagonists: when η is the maximum, the corresponding C_t is significantly degraded. In contrast, when C_t is enhanced, η is reduced. This corresponds to the following operational situations: in cruising flight, it is desirable to optimize the propulsive efficiency in order to increase the autonomy of the vehicle. Also, to improve maneuverability and acceleration, it is required to maximize thrust.

To solve this intricate problem, researchers have recently focused on the application of optimization techniques to choose the best control parameters leading to optimal efficiency with acceptable thrust force.

Tuncer and Kaya (2005) performed an optimization of both the flapping airfoil thrust and the propulsive efficiency by using a gradient-based optimization method. The parallel computation and the multi-objective optimization are performed at $Re = 1 \times 10^4$ and $M = 0.1$. Using the heaving and pitching amplitudes, h_0 and θ_0 respectively, and the phase angle φ as optimization parameters, they obtained a maximum propulsive efficiency $\eta_{\max} = 67.5\%$ with $C_{\mathrm{t}} = 0.18$, and a maximum thrust coefficient $C_{\mathrm{tmax}} = 1.41$ with $\eta = 28.3\%$ for different values of the control parameters.

Yang *et al.* (2006) maximized the propulsive efficiency and the time-averaged thrust coefficient using a 3D unsteady compressible Euler/Navier-Stokes flow solver for an NACA0012 airfoil with combined sinusoidal pitching and plunging motions. They obtained an optimal efficiency value $\eta_{\max} = 90\%$ with $C_{\mathrm{t}} = 0.24$, and a maximum thrust value $C_{\mathrm{tmax}} = 0.86$ with $\eta = 65\%$.

Kaya and Tuncer (2006) solved the same problem stated in Tuncer and Kaya (2005), but with the flapping motion described by non-uniform B-spline. This results in a significant improvement over sinusoidal motion. Later, Kaya and Tuncer (2008a; 2008b) employed the response surface methodology (RSM) to optimize the thrust generated by both a single and a dual airfoil undergoing flapping motion with path based on a parametric 3rd degree non-uniform rational B-splines function. They established that the optimization process with RSM is about one order of magnitude more efficient and robust in comparison to the gradient based optimization process. In addition, they found that the number of unsteady flow runs is significantly smaller in the RMS than in the gradient method. Soueid *et al.* (2009) optimized the kinematics of a flapping airfoil using numerical simulations at a low Re value of 1.1×10^3. The problem was solved using steepest descent and quasi-Newton methods. This study also corroborates the conclusions of Anderson *et al.* (1998), which stated that the high propulsive efficiency occurs when (1) the reverse Von Kármán street is observed, (2) the Strouhal number (S_{t}) is close to 0.2, and (3) the phase angle between the heaving and pitching motions is equal to 90°.

In the present paper, we consider the problem of propulsive efficiency optimization of a 2D plunging, 80 mm chord length NACA0012 airfoil for three fluid speed values, $U_0 = 0.6,\ 2.0$, and 4.0 m/s, which correspond to $Re = 3.3 \times 10^3$, 1.1×10^4, and 2.2×10^4, respectively. The reduced frequency and the plunging amplitude are considered as the control parameters of the applied sinusoidal motion. The unsteady laminar flow over a rigid airfoil undergoing sinusoidal plunging motion is computed using the commercial ANSYS FLUENT 12.0 computational fluid dynamics (CFD) package. An inhouse user defined function (UDF) is used to handle the desired airfoil motion. Using an RSM, the propulsive efficiency is optimized for maximum thrust generation or input power minimization. Although the adopted laminar flow assumption at small plunge amplitudes and high frequencies cannot represent faithfully the wake configuration, as mentioned by Young and Lai (2004), the quantitative results still remain valid. A judicious exploitation of the constructed response surfaces is given in order to setup the adequate control motion parameters ensuring the best performance compatible with the operational requirements. It is established that operating at a fixed high efficiency level is possible under two main interesting configurations: (1) high thrust forces by setting high frequency, and (2) low input power by adopting low motion amplitude.

2 Scaling and kinematics parameters

Two non-dimensional parameters, a reduced frequency, and a non-dimensional plunging amplitude, are used in this study to characterize the plunging airfoil performance.

2.1 Reduced frequency and plunging amplitude

The reduced frequency is defined in Platzer *et al.* (2008) as

$$k = \frac{2\pi f c}{U_0}, \tag{1}$$

where f is the oscillation frequency, c is the airfoil chord length, and U_0 is the mean forward velocity. The parameter k characterizes the unsteady property of the flapping motion, that is, flow separation and leading-edge shedding effects (Young and Lai, 2007). It is worth mentioning that the Strouhal number can be used together with the reduced frequency.

The Strouhal number is defined in Anderson

et al. (1998) as

$$S_{\mathrm{t}} = \frac{fA}{U_0} = \frac{1}{\pi} k h_0, \tag{2}$$

where A denotes the width of the wake, which is approximated with the peak-to-peak maximum excursion of the trailing edge of the airfoil.

Both S_{t} and k must be considered simultaneously to study the flapping foil performance (Isogai *et al.*, 1999; Ramamurti and Sandberg, 2001). As mentioned in Lian and Shyy (2007) and Young and Lai (2004; 2007), the wake structure pattern and the aerodynamic performance of a plunging airfoil are strongly dependent on the values of these two parameters (i.e., S_{t} and k) that describe both the temporal and spatial properties of the flapping motion.

In the present study, the considered NACA0012 airfoil undergoes a simple harmonic plunging motion defined as

$$\frac{h(t)}{c} = h_0 \sin(2\pi f t), \tag{3}$$

where $h(t)$ and h_0 denote the instantaneous position and the dimensionless amplitude, respectively.

2.2 Plunging motion kinematics

Using Eq. (3), the vertical velocity of the airfoil due to the plunging motion is given by

$$\frac{\mathrm{d}h(t)}{\mathrm{d}t} = 2\pi f c h_0 \cos(2\pi f t). \tag{4}$$

The kinematic angle of attack (AoA) $\alpha(t)$, which is induced by the flapping motion, is a derivative parameter of crucial importance for the airfoil performance. It is given by Lian and Shyy (2007) by the following relations:

$$\alpha(t) = \arctan\left(\frac{\mathrm{d}h(t)}{\mathrm{d}t}\frac{1}{U_0}\right), \tag{5}$$

or

$$\alpha(t) = \arctan(\pi S_{\mathrm{t}} \cos(2\pi f t)). \tag{6}$$

Eq. (6) shows the direct effect of Strouhal number on the control of the AoA during the airfoil motion. Fig. 1 illustrates the time evolution of the kinematic parameters of the airfoil obtained for $k = 2.51$, $h_0 = 0.25$, and $Re = 1.1 \times 10^4$.

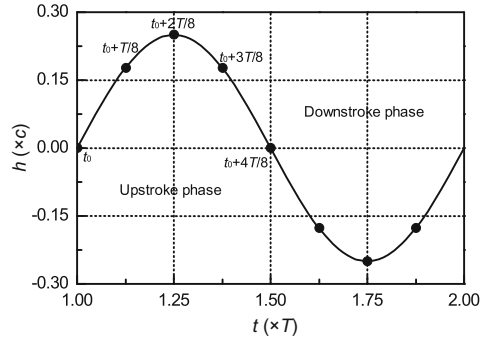

(a)

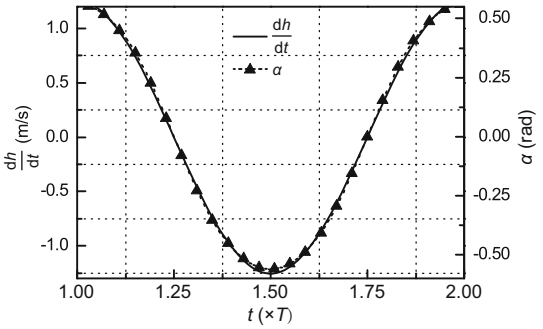

(b)

Fig. 1 Kinematic parameters of the airfoil for $k = 2.51$, $h_0 = 0.25$, and $Re = 1.1 \times 10^4$
(a) Instantaneous plunging amplitude; (b) Angle of attack. c is the airfoil chord length and T is the period of oscillation

2.3 Definition of the thrust coefficient and propulsive efficiency

The time-averaged value of the generated thrust force for a motion performed during a period $T = 1/f$ is defined as

$$\overline{F} = \frac{1}{T}\int_0^T X(t)\mathrm{d}t, \tag{7}$$

and the mean mechanical input power $\overline{P}$ required to maintain the heave motion is given by

$$\overline{P} = \frac{1}{T}\int_0^T Y(t)\frac{\mathrm{d}h(t)}{\mathrm{d}t}\mathrm{d}t, \tag{8}$$

where $X(t)$ and $Y(t)$ represent the instantaneous drag and lift forces, respectively.

The mean thrust coefficient $\overline{C_{\mathrm{t}}}$ is defined as

$$\overline{C_{\mathrm{t}}} = -\frac{\overline{F}}{\frac{1}{2}\rho S U_0^2} = -\frac{1}{T}\int_0^T C_{\mathrm{d}}(t)\mathrm{d}t, \tag{9}$$

and the mean input power coefficient $\overline{C_{\mathrm{P}}}$ is defined

as

$$\overline{C_{\mathrm{P}}}=\frac{\overline{P}}{\frac{1}{2}\rho SU_0^3}=\frac{2\pi fh_0c}{TU_0}\int_0^T C_{\mathrm{l}}(t)\cos(2\pi ft)\mathrm{d}t, \tag{10}$$

where ρ stands for fluid density, $S=c\times 1$ for area of the airfoil, $C_{\mathrm{d}}=X/(\frac{1}{2}\rho SU_0^2)$ for drag coefficient, and $C_{\mathrm{l}}=Y/(\frac{1}{2}\rho SU_0^2)$ for lift coefficient.

The propulsive efficiency is defined by

$$\eta=-\frac{\overline{F}U_0}{\overline{P}}=\frac{\overline{C_{\mathrm{t}}}}{\overline{C_{\mathrm{P}}}}. \tag{11}$$

This definition loses its physical meaning when the airfoil produces drag (i.e., $\eta<0$).

From the developed mathematical formulations (Eqs. (3)–(11)), it appears that the propulsive efficiency of an oscillating wing is determined by an appropriate choice of kinematic motion parameters. In our case, the performance of the airfoil depends on three parameters: the Strouhal number, the heaving amplitude, and the Reynolds number.

3 Numerical methods

3.1 Navier-Stokes solver

To compute the unsteady viscous flow-fields around a plunging NACA0012 airfoil, 2D numerical simulations were carried out using the commercial code ANSYS FLUENT 12.0. The incompressible Navier-Stokes equations are solved using the finite volume method on a body conformal moving grid. For spatial discretization, the convective flux is evaluated using a second-order upwind scheme while the diffusive flux is evaluated via second-order central differences. The pressure-velocity coupling is handled by means of the SIMPLEC algorithm. In all simulations, the flow is considered to be laminar. The plunging airfoil motion assumes the foil as a rigid body. For that purpose, the airfoil and the neighbouring computational grid region are moved using the dynamic mesh module along with an in-house UDF. This module uses a first-order implicit scheme for temporal discretization. The mesh update is performed at each time step on the basis of the new boundary position. The developed UDF allows the calculation of the position of each point of the moving wall at the beginning of each iteration.

Neglecting the added mass effect, i.e., inertial force of the air displaced by the airfoil, the instantaneous force produced by the flapping airfoil is evaluated by integration of the airfoil pressure and strain rate distributions.

3.2 Grid generation

The numerical result accuracy is affected by the grid size, as the dynamic mesh technique is used and the pressure values on the airfoil wall are integrated to calculate the aerodynamic forces generated by the oscillations. According to the strategy proposed by Isogai *et al.* (1999) and Miao and Ho (2006), the computational domain is divided into two zones (Fig. 2). The first zone contains the airfoil with a structured mesh in order to accurately capture the gradients in the boundary layer. In the second zone an unstructured mesh is used. This strategy makes it possible to keep the same grid around the airfoil during the entire simulation. In Zone 1, the first grid point is located at a normal distance y_p corresponding to a wall Yplus value $y^+\simeq\rho u_\tau y_p/\mu=1$ (Münch *et al.*, 2010), where $u_\tau=\sqrt{\tau_{\mathrm{w}}/\rho}$ is the friction velocity, $\tau_{\mathrm{w}}=0.322\rho U_0^2/\sqrt{Re}$ is the wall shear stress, and μ is the viscosity.

Note that the interface between the two regions is modeled as conformal type cell to ensure flux conservation for all variables without degrading the flow field. The dimensions of the computational domain and the boundary conditions are given in Fig. 2.

3.3 Mesh and time-step refinement

The numerical solution accuracy is checked via additional calculations which are carried out for $Re=1.1\times10^4$ with control parameter values $k=2.01$ and $h_0=0.375$. To assess grid convergence, several grids have been used. The height of the mesh cells in contact with the airfoil wall is given in the second column of Table 1. All tested grids have 2×82 points on the airfoil surface and are tested with a time step $\mathrm{d}t=T/100$.

The time variation of drag and lift coefficients, C_{d} and C_{l} respectively, which is shown in Fig. 3 reveals that Grids 1 and 2 poorly estimate the drag coefficient resulting in an underestimation of $\overline{C_{\mathrm{d}}}$ (Table 1). On the other hand, Grids 3 and 4 provide similar values of $\overline{C_{\mathrm{d}}}$. Grid 3 provides a good compromise between accuracy and computational burden,

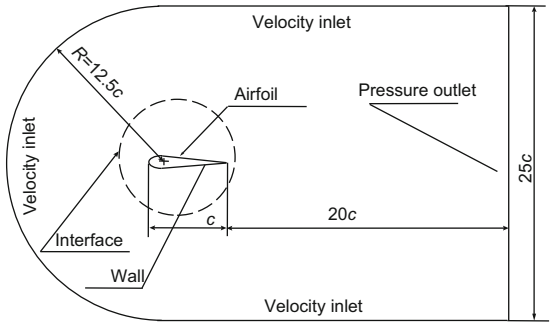

(a)

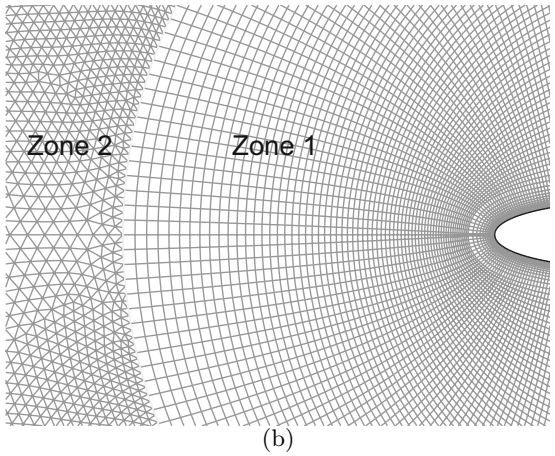

(b)

Fig. 2 Computational domain (a) and conformal hybrid mesh system (b) for plunging airfoil

Table 1 Tested grid properties

Grid	First grid row distance	Number of nodes	$\overline{C_\mathrm{d}}$	C_{dsteady}
1	$0.0361c$	11 156	-0.061	
2	$0.0048c$	15 271	-0.180	0.036
3	$0.0012c$	44 850	-0.202	
4	$0.0006c$	74 777	-0.202	

and as a result is chosen to perform the numerical simulations.

Another study is carried out to check the stability of the solution with respect to the time step. We consider seven time step values, namely: $\mathrm{d}t1 = T/10$, $\mathrm{d}t2 = T/20$, $\mathrm{d}t3 = T/40$, $\mathrm{d}t4 = T/80$, $\mathrm{d}t5 = T/100$, $\mathrm{d}t6 = T/120$, and $\mathrm{d}t7 = T/200$. Fig. 4 displays the time evolution of both C_d and C_l, which shows that $\mathrm{d}t = T/100$ is sufficient for time accuracy. Furthermore, this choice of time step provides stable remeshing calculations.

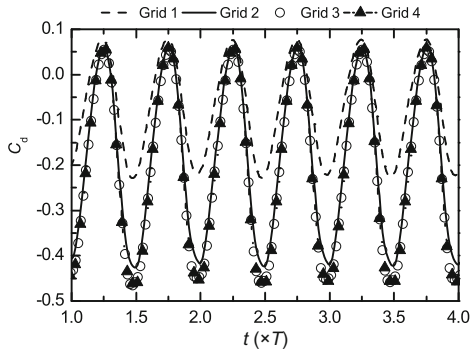

(a)

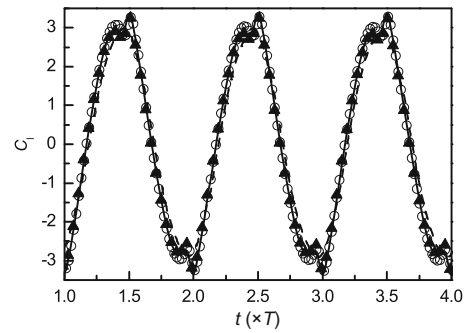

(b)

Fig. 3 Temporal evolution of drag (a) and lift (b) coefficients for tested grids

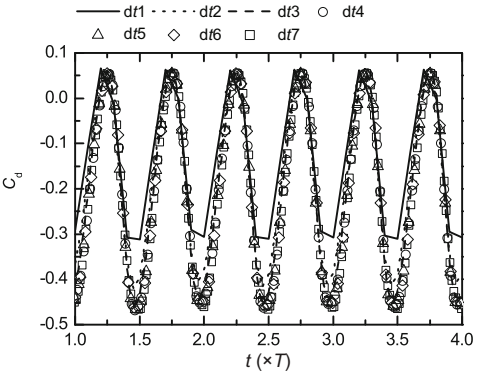

(a)

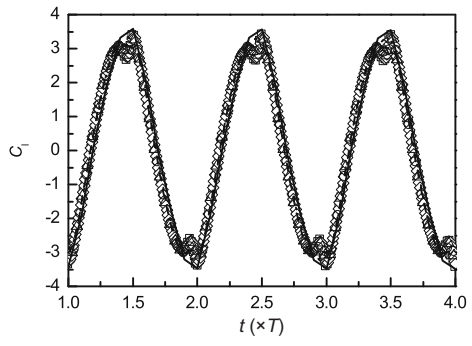

(b)

Fig. 4 Temporal evolution of drag (a) and lift (b) coefficients for tested time step values

3.4 Solver validation

In order to validate the Navier-Stokes computational solver, preliminary simulations at $Re = 1\times10^4$ are performed. Mean average values of thrust, input power, and propulsive efficiency are calculated for the following plunging parameters: $h_0 = 0.125$, 0.175, and 0.250, and a Strouhal number varying in the interval $[0, 0.5]$. The obtained values, which are shown in Fig. 5, are compared with those obtained by the potential theory (Garrick, 1936), as well as experimental and numerical results performed by Young and Lai (2004) and Heathcote *et al.* (2008).

In the present study, the solution is assumed convergent when the change of both thrust coefficient and propulsive efficiency, during two successive cycles does not exceed 1%. Under this condition, the periodic solution is attained after four cycles, a result which agrees well with Isogai *et al.* (1999) and Miao and Ho (2006). The time-averaged force $\overline{F}$ and the time-averaged power $\overline{P}$ are computed over n flapping periods starting from the converged solution via

$$\overline{F} = \frac{1}{nT}\int_0^{nT} X(t)\mathrm{d}t,\quad \overline{P} = \frac{1}{nT}\int_0^{nT} Y(t)\frac{\mathrm{d}h(t)}{\mathrm{d}t}\mathrm{d}t. \tag{12}$$

The calculations were performed on a workstation equipped with an Intel Xeon E5405, 2 GHz CPU, and 4 GB of RAM. For $n = 10$, the CPU time is about 5 h for each simulation.

As shown in Fig. 5, our results are in good agreement with the reported experimental and numerical results. This is quite true for propulsive efficiency. However, Garrick's potential theory overestimates the thrust coefficient. As mentioned by Platzer *et al.* (2008), this may be explained, by the fact that Garrick's analysis considers non-viscous flow, while a Navier-Stokes calculation gives a negative thrust, i.e., a viscous drag, for very low Strouhal number values.

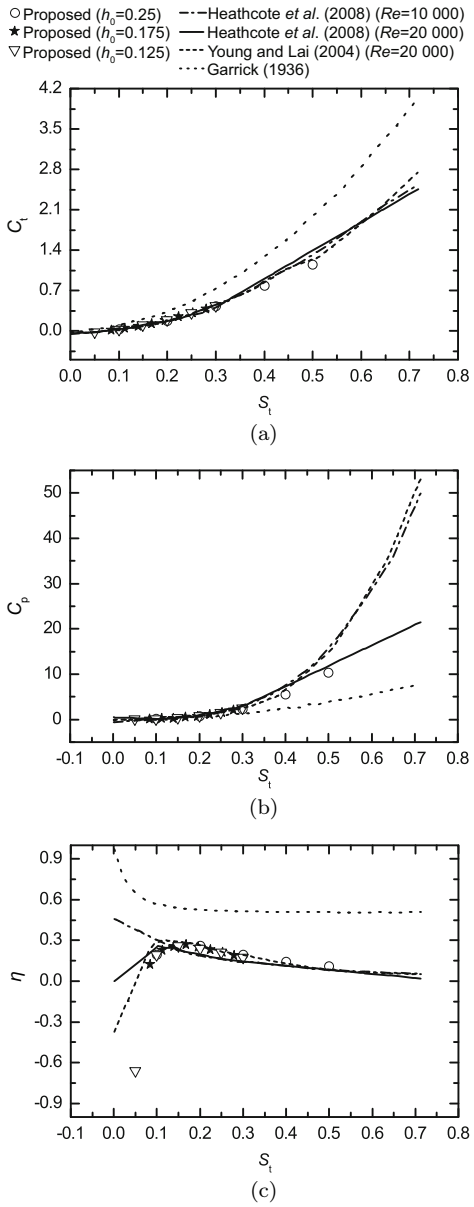

Fig. 5 Navier-Stokes solver result validation against theoretical (Garrick, 1936), experimental (Heathcote *et al.*, 2008) and numerical (Young and Lai, 2004) data

(a) Thrust coefficient; (b) Input power coefficient; (c) Propulsive efficiency

4 Optimization approach

In order to maximize the propulsive efficiency (Eq. (11)) of a plunging NACA0012 airfoil, an optimization technique based on the RSM is considered. RSM is an approximation based optimization method that is able to find good solutions for complex engineering optimization problems by calculating specific values of the objective function for various combinations of the optimization variables (Raymer, 2002; Box and Draper, 2007). Indeed, this method has been successfully applied for solving intricate engineering problems (Haftka *et al.*, 1998; Wang and Dong, 2000; Raymer, 2002; Rodriguez, 2003). The common point to all these problems is the fact that inherent merit

functions generally involve both intensive and expensive numerical/experimental tests. However, the number of tests required for the optimization process should be minimized. RSM consists of experimental methods in which all optimization variables are discretized either according to a simple parametric scheme or using a given experimental planning, such as factorial design, orthogonal design, or central composite design (Box and Draper, 2007).

The response surface is an approximation model for the relationship between optimization variables and the objective function. Generally, linear or quadratic polynomial methods are built by means of the least-squares method. Once the surface response is available, conventional optimization techniques, such as gradient-based techniques or global optimization techniques, may be applied to estimate the function's optimal point by searching in the constructed surface. The accuracy of the obtained optimal value naturally depends on the selected design and the adopted fitting model.

The optimization problem considered in this study involves expensive computer calculations. Thus, RSM is suitable for its treatment. In our study, and for a fixed value of Re, the RSM is applied according to the approach illustrated in the flowchart of Fig. 6.

Following the problem statement discussed in Section 2, we first identify the heaving amplitude h_0 and the reduced frequency k as the main optimization variables while the system propulsion efficiency η is assumed to be the response. The study of the related bibliography allows us to define the following interest region: $[h_{0\min} - h_{0\max}][k_{\min} - k_{\max}] = [0.125 - 0.375][1.26 - 7.54]$. Furthermore, since we only have two optimization variables, a balanced multilevel design with at least five levels for each factor is initially adopted. Numerical simulations are conducted using the ANSYS FLUENT and according to the solver elaborated in Section 3. An initial surface response is constructed using a polynomial fitting model. Then, using a Nelder-Mead algorithm, the optimum point of the surface is easily found. The Nelder-Mead simplex method is a direct search approach used to minimize the considered objective function. The algorithm of the Nelder-Mead method can be described as follows (Yang *et al.*, 2005):

1. Set three initial estimates of the position of the minimum x_1, x_2, and x_3, where $\eta(x_1) < \eta(x_2) < \eta(x_3)$.

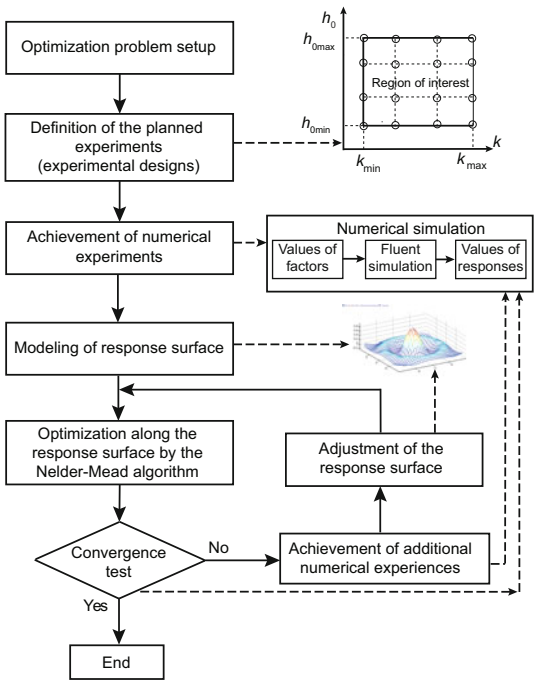

Fig. 6 Diagram of the response surface methodology

2. If the three points or their function values are sufficiently close to each other, then declare x_1 to be the minimum and terminate the procedure.

3. Otherwise, expecting that the minimum we are looking for may be at the opposite side of the worst point x_3 over the line $\overline{x_1x_3}$, take

$$x_4 = x_5 + 2(x_5 - x_3), \text{ where } x_5 = (x_1 + x_2)/2,$$

and if $\eta(x_4) < \eta(x_2)$, take x_4 as the new x_3; otherwise, take

$$x_6 = (x_5 + x_4)/2 = 2x_5 - x_3;$$

and if $\eta(x_6) < \eta(x_3)$, take x_6 as the new x_3; if $\eta(x_6) \geq \eta(x_2)$, take

$$x_7 = (x_3 + x_5)/2;$$

and if $\eta(x_7) < \eta(x_3)$, take x_7 as the new x_3; otherwise, give up the two points x_2, x_3 and take x_5 and $x_8 = (x_1 + x_3)/2$ as the new x_2 and x_3, reflecting our expectation that the minimum would be around x_1.

4. Go back to Step 1.

The remaining steps of the proposed RSM-based optimization approach aim at enhancing the quality of the obtained optimal design. Additional numerical tests are conducted to obtain additional response

surfaces until a convergence criterion is satisfied. If the difference between the optimum value obtained from the surface response and the value obtained via the numerical simulation reaches a given threshold, the optimization process is stopped.

5 Results and discussion

Before starting the numerical results analysis of the optimization process, a qualitative study of the flow field around the plunging airfoil is presented for a representative case. This study is conducted over one plunging cycle by monitoring the evolution of the aerodynamic force coefficients and the pressure distribution around the airfoil in connection to the plunging kinematics. Exhaustive study of the laminar separation bubbles for such Reynolds numbers is widely reported (Sane, 2003; Lian and Shyy, 2007; Bansmer *et al.*, 2010).

The considered case is characterized by $Re = 1.1 \times 10^4$, $k = 2.51$, and $h_0 = 0.25$. The kinematics of the airfoil is illustrated in Fig. 1 and the induced aerodynamic forces are given in Fig. 7.

5.1 Aerodynamic coefficients

Fig. 7 illustrates the evolution of the aerodynamic coefficients corresponding to the airfoil kinematics of Fig. 1. The drag coefficient frequency is twice the lift coefficient frequency. Also, Fig. 7 shows the Knoller-Betz effect which states that the airfoil produces aerodynamic forces by achieving a sinusoidal distribution of AoA (Platzer *et al.*, 2008).

It is worth noting that when the reduced frequency k becomes close to the threshold value 0.5 (Lian and Shyy, 2007), the unsteady effect governs the aerodynamic force generation and a hysteresis of the lift coefficient appears. In addition, as shown in Fig. 7, the drag coefficient C_d follows the kinematics of AoA, but a significant phase shift exists between lift and drag coefficients.

5.2 Pressure distribution

The qualitative behavior of the wake is presented using a laminar solver without turbulence modeling. This might be unrealistic, especially at small plunge amplitudes and high frequencies (Young and Lai, 2004). Nevertheless, several researchers have numerically studied the thrust generation mechanism using turbulence models (Isogai *et al.*, 1999; Young and Lai, 2004; Tuncer and Kaya, 2005; Münch *et al.*, 2010).

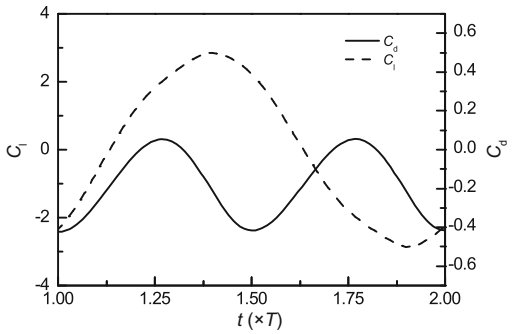

Fig. 7 Drag and lift coefficients history of a plunging NACA0012 airfoil for $k = 2.51$, $h_0 = 0.250$, and $Re = 1.1 \times 10^4$

The observations are done over eight airfoil successive positions, which are shown as black circles in Fig. 1a. Figs. 8–12 displays the variation of the pressure distribution induced by the instantaneous AoA on the upper and lower airfoil sides over one plunging cycle. Eight airfoil successive positions are considered to tackle both the flow evolution and induced modifications.

The upstroke begins at $t = t_0$ (Fig. 8). The airfoil is at the first selected position and starts moving upward. The pressure differences between the upper and lower sides of the airfoil is much larger than that obtained for the same static airfoil at zero incidence. The stagnation point (Fig. 8b), which is at the stroke beginning of the leading edge, moves upward and stabilizes slightly downstream on the airfoil upper surface. The streamlines at this point of the cycle are outgoing for the airfoil upper surface and incoming for the lower surface. A vortex generated during the previous stroke is evolving contiguously to the upper airfoil side and reaches the trailing edge to be shed in the airfoil wake (Fig. 8c). At these times and positions, the lift and drag coefficients coincide with their local minimum values (Fig. 7).

At the step of the stroke where $t = t_0 + T/8$, the airfoil is moving upward (Fig. 9). A primary leading edge vortex (LEV) is formed, followed by a secondary additional small vortex (Fig. 9b). The two co-rotating vortices evolve counterclockwise. The suction region translates with the travelling LEV on the airfoil upper surface and the corresponding aerodynamic forces are substantially reduced.

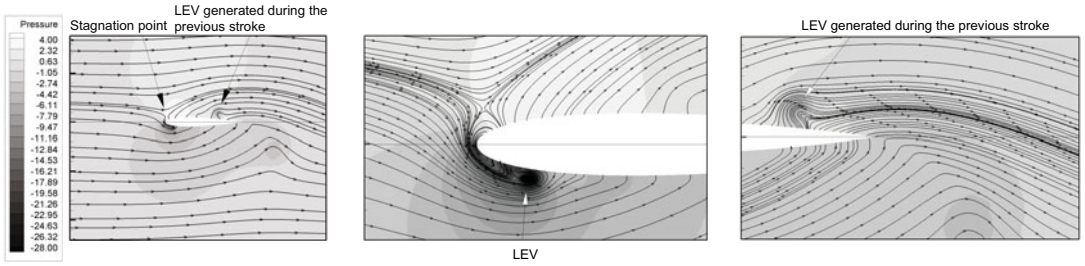

Fig. 8 Pressure distribution at $t = t_0$, $Re = 1.1 \times 10^4$, $k = 2.51$ and $h_0 = 0.250$. (a) Variation of the pressure; (b) Leading edge zoom; (c) Trailing edge zoom. LEV: Leading edge vortex; Pressure unit: Pa

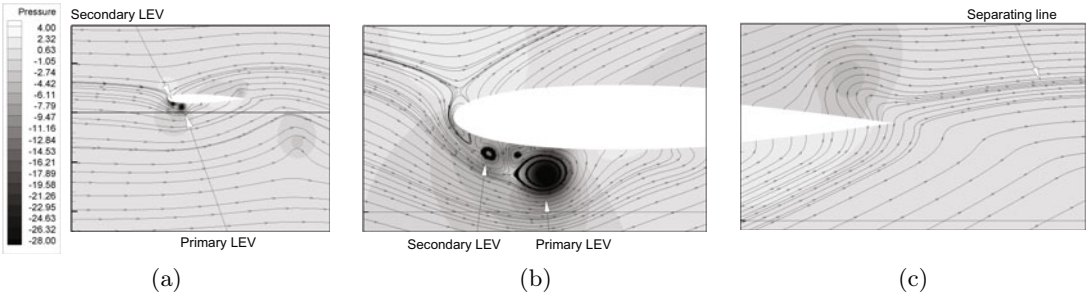

Fig. 9 Pressure distribution at $t = t_0 + T/8$, $Re = 1.1 \times 10^4$, $k = 2.51$ and $h_0 = 0.250$. (a) Variation of the pressure; (b) Leading edge zoom; (c) Trailing edge zoom. LEV: Leading edge vortex; Pressure unit: Pa

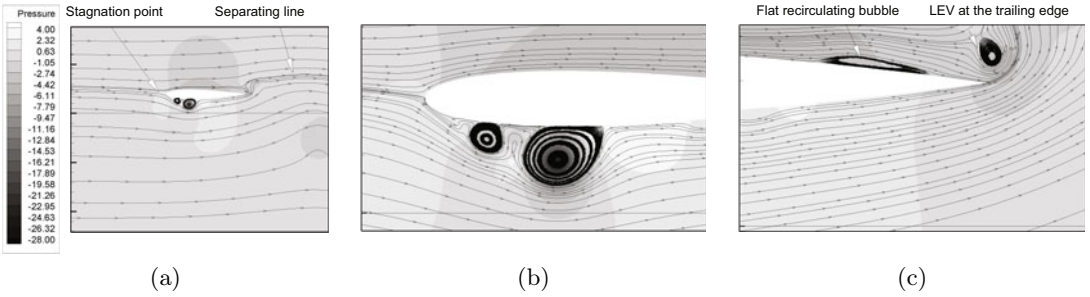

Fig. 10 Pressure distribution at $t = t_0 + 2T/8$, $Re = 1.1 \times 10^4$, $k = 2.51$ and $h_0 = 0.250$. (a) Variation of the pressure; (b) Leading edge zoom; (c) Trailing edge zoom. LEV: Leading edge vortex; Pressure unit: Pa

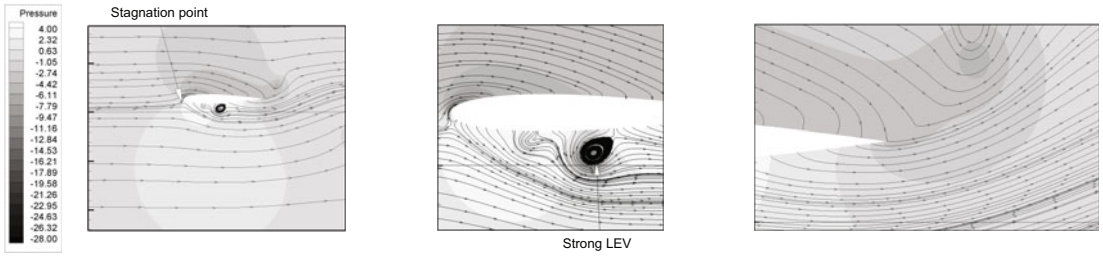

Fig. 11 Pressure distribution at $t = t_0 + 3T/8$, $Re = 1.1 \times 10^4$, $k = 2.51$ and $h_0 = 0.250$. (a) Variation of the pressure; (b) Leading edge zoom; (c) Trailing edge zoom. LEV: Leading edge vortex; Pressure unit: Pa

Furthermore, the stagnation point at the leading edge shifts slightly downstream on the airfoil upper surface (Fig. 9b). Likewise, at the trailing edge, the separating line between extrados and intrados flows (Fig. 9c) moves in the upward direction with a slight distortion on the airfoil surface.

At $t = t_0 + 2T/8$ (Fig. 10), the stagnation point returns to its initial position in front of the leading edge (Fig. 10b) and the streamlines are parallel to the upper surface of the airfoil. A relative flat recirculating bubble (Fig. 10c), which evolves contiguously to the upper surface at the trailing edge, results in a pressure gradient, which promotes a maximal aerodynamic force (thrust and lift). A vortex originating from the previous stroke reaches the trailing edge and is about to leave the airfoil for the wake (Fig. 10c). The strengthening of the LEV contributes to the increase of the aerodynamic force coefficient.

At $t = t_0 + 3T/8$ (Fig. 11), the stagnation point moves slightly to the lower surface side (Fig. 11b). The streamlines clearly show that the vortex displacement is accompanied by a continuous rotating movement along the airfoil lower surface (Fig. 11b). The flow separates as it passes through the separation zone, but reattaches before it reaches the trailing edge to maintain the Kutta condition (Fig. 11b). The pressure profiles show both a pressure-drop zone located at the airfoil upper surface and a higher pressure zone on the lower airfoil surface away from the vortex area. This flow configuration is physically favorable to the enhancing of the airfoil lift force.

At $t = t_0 + 4T/8$ (Fig. 12), the airfoil comes back to the median position with negative speed. The airfoil starts its downstroke phase where the pressure field pattern and the vortex evolution are spatiotemporally symmetric with respect to the upstroke phase.

5.3 Optimization results

The numerical simulations are carried out for three Re values: 3.3×10^3, 1.1×10^4, and 2.2×10^4.

Fig. 13 shows the evolution of both thrust coefficient and efficiency versus Reynolds number at $h_0 = 0.125$ and $k = 3.77$. The steep increase of η when $Re \in [3.3 \times 10^3 , 1.1 \times 10^4]$ and its moderate increase when $Re \in [1.1 \times 10^4 , 2.2 \times 10^4]$ are due to the variation of C_t with a same order of magnitude as that of η. In other words, the mean power required to sustain the airfoil motion remains nearly constant

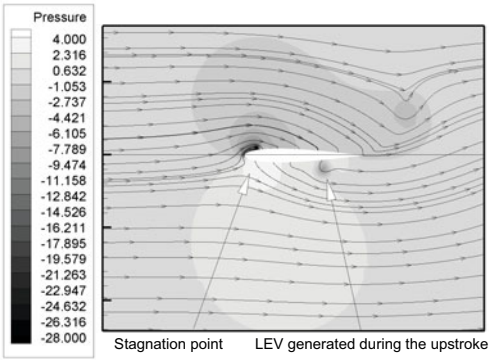

Fig. 12 Pressure distribution at $t = t_0 + 4T/8$, $Re = 1.1 \times 10^4$, $k = 2.51$ and $h_0 = 0.250$. LEV: Leading edge vortex; Pressure unit: Pa

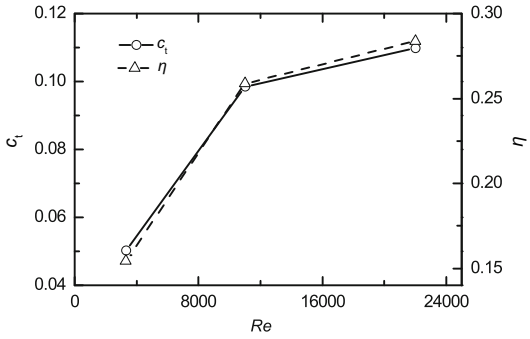

Fig. 13 Propulsive efficiency and thrust coefficient versus Reynolds number for $k = 3.77$ and $h_0 = 0.125$

in the range of the Reynolds numbers of the present study.

The first optimization level, which corresponds to the first constructed response surface, is performed with the following initial interest region $[h_{0\min} - h_{0\max}][k_{\min} - k_{\max}] = [0.125 - 0.375][1.26 - 7.54]$. The calculated airfoil performances in terms of thrust, input power, and propulsive efficiency are plotted in Figs. 14–16, respectively. It is observed that the thrust coefficient and the input power efficient increase with k. However, for higher values of k, C_p increases faster than C_t, and a lower propulsive efficiency is obtained.

The data in Fig. 16 is used to build initial response surfaces in terms of the propulsive efficiency. These surfaces are built using a quadratic function of the following form:

$$\mathfrak{f}(x, y) = a_0 + a_1 x + a_2 y + a_3 xy + a_4 x^2 + a_5 y^2, \quad (13)$$

where the constants a_i ($i = 0,1,2,3,4,5$) are evaluated via a least-squares method (Yang *et al.*, 2005). An approximation of the optimal propulsive efficiency

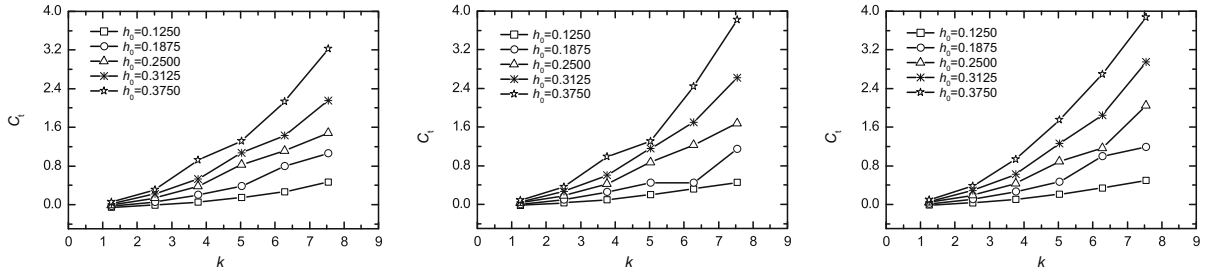

(a) (b) (c)

Fig. 14 Thrust coefficient C_t for various Reynolds number values. (a) $Re = 3.3 \times 10^3$; (b) $Re = 1.1 \times 10^4$; (c) $Re = 2.2 \times 10^4$

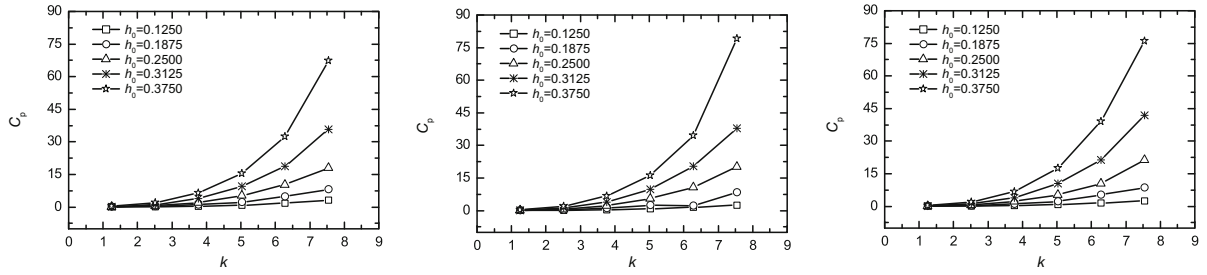

(a) (b) (c)

Fig. 15 Input power efficient C_p for various Reynolds number values. (a) $Re = 3.3 \times 10^3$; (b) $Re = 1.1 \times 10^4$; (c) $Re = 2.2 \times 10^4$

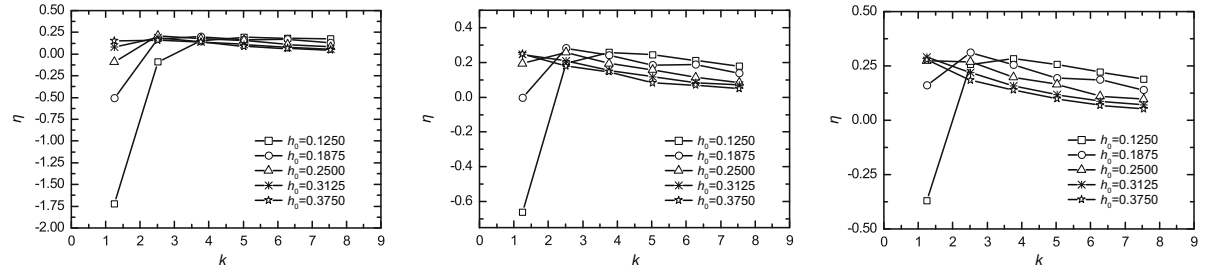

(a) (b) (c)

Fig. 16 Propulsive efficiency η for various Reynolds number values. (a) $Re = 3.3 \times 10^3$; (b) $Re = 1.1 \times 10^4$; (c) $Re = 2.2 \times 10^4$

value η_{app} is obtained using the Nelder-Mead algorithm (Yang *et al.*, 2005), which finds the global maximizer of the constructed surfaces. For the control parameters (i.e., h_0 and k) yielding η_{app}, an additional numerical simulation is conducted to get η_{sim}, which is compared to η_{app}. The convergence criterion in Eq. (14) decides if a new response surface is needed or not:

$$\xi = \| \frac{\eta_{\text{sim}} - \eta_{\text{app}}}{\eta_{\text{sim}}} \| \leq 1. \tag{14}$$

In case a new surface is needed, the interest region is systematically reduced and additional experiments are planned around the latest point found for the evaluation of η_{app} (Fig. 6). In this study, only two additional surfaces have been constructed until convergence is reached. Fig. 17 illustrates the three response surfaces obtained at the last optimization level with a final interest region range $[h_{0\min} - h_{0\max}][k_{\min} - k_{\max}] = [0.125 - 0.25][1.26 - 5.03]$. Tables 2–4 summarize the main numerical results obtained during the whole optimization process. The best combination of control parameters corresponds to the optimal point (OP). This is clearly highlighted in Fig. 18.

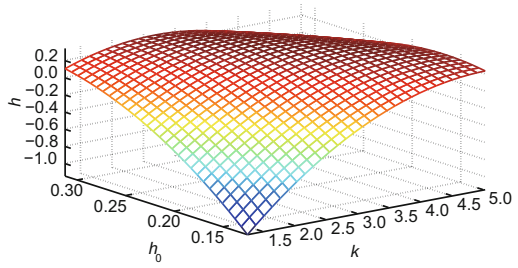

(a)

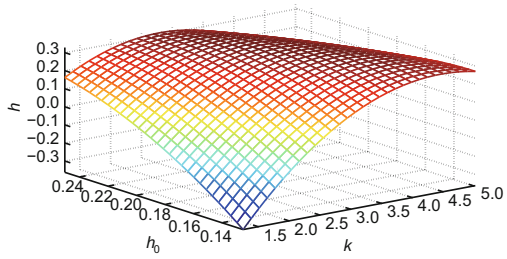

(b)

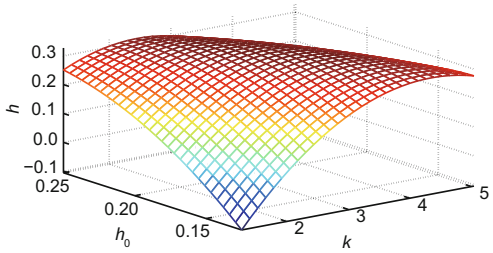

(c)

Fig. 17 Approximated response surfaces at the 3rd optimization level: (a) $Re = 3.3 \times 10^3$; (b) $Re = 1.1 \times 10^4$; (c) $Re = 2.2 \times 10^4$

The 2D contours of the approximated surfaces are shown in Fig. 18. We noted that different h_0 and k combination values yield the same propulsive efficiency. This fact may be exploited judiciously in practice. For example, in order to increase the autonomy of a mechanical flapping vehicle, it is preferable to adopt a combination of h_0 and k that minimizes C_p. In contrast, to improve maneuverability and acceleration, it is required to maximize C_t. These two cases are guaranteed for the same η value. Furthermore, a compromise between these two extreme situations is also possible, while keeping the same efficiency level.

Now we provide a simple way to select the adequate combination. First, choose the contour level surrounding the OP with a propulsive efficiency value close to η_app (Fig. 18). Then draw a horizontal line and a vertical line passing through OP. The intersection of the two lines with the selected contour level defines four characteristic points denoted: north, south, east, and west points (NP, SP, EP, and WP). Note that, NP and SP have the same k, while EP and WP have the same h_0.

Table 2 Optimum evolution through the optimization process at $Re = 3.3 \times 10^3$

Level	f (Hz)	k	h_0	η_app (%)	η_sim (%)	ξ (%)
1	3.49	2.922	0.213	29.4	21.2	39.20
2	2.34	1.963	0.322	20.2	19.4	3.76
3	3.25	2.720	0.245	21.6	21.5	0.05

Table 3 Optimum evolution through the optimization process at $Re = 1.1 \times 10^4$

Level	f (Hz)	k	h_0	η_app (%)	η_sim (%)	ξ (%)
1	12.26	1.257	0.347	25.4	25.3	0.67
2	5.00	2.118	0.216	30.4	27.2	11.6
3	8.43	2.208	0.221	28.1	27.9	0.83

Table 4 Optimum evolution through the optimization process at $Re = 2.2 \times 10^4$

Level	f (Hz)	k	h_0	η_app (%)	η_sim (%)	ξ (%)
1	24.02	3.018	0.128	31.6	29.6	1.07
2	21.36	2.684	0.159	32.5	31.0	4.61
3	16.18	2.034	0.219	31.2	30.9	6.75

Additional calculations are performed for these points and the obtained performance results are summarized in Tables 5–7. The prediction error for the propulsive efficiency η is generally less than 2%.

Furthermore, a close examination of the results in Tables 5–7 reveals that, whatever the Reynolds numbers:

1. C_tmax is always recorded at EP, which is characterized by a high frequency;

2. C_pmin is always recorded at SP, which is characterized by a low amplitude;

3. NP and WP give a compromise between maximizing C_t and minimizing C_p;

4. A higher thrust value is achievable with control parameters leading to the largest Strouhal number.

The obtained results corroborate those of Young and Lai (2007), which indicate that for an imposed S_t, it is more beneficial to operate at high k and low h_0 rather than at low k and high h_0.

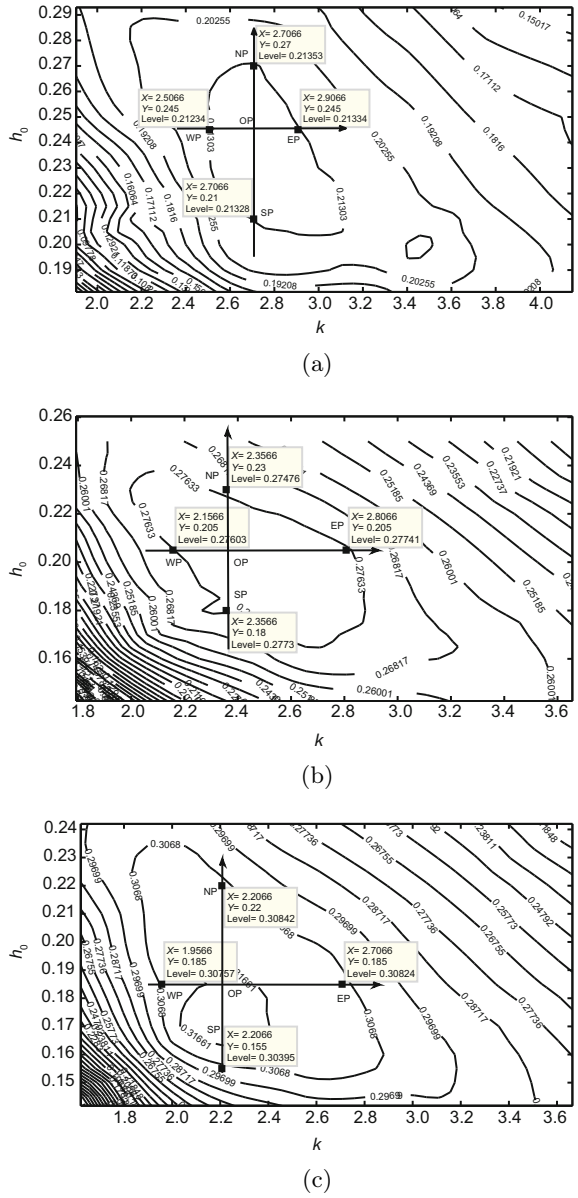

Fig. 18 Efficiency contours for $Re = 3.3 \times 10^3$ (a), $Re = 1.1 \times 10^4$ (b), and $Re = 2.2 \times 10^4$ (c)

The salient feature of the proposed approach, in contrast to previous works (Kaya and Tuncer, 2006; 2008a; Soueid *et al.*, 2009), is the fact that all the results of the optimization process are stored implicitly in the constructed response surface and they are used to define the characteristics points (NP, SP, EP, and WP) for a given fixed efficiency level without conducting additional simulation. Indeed, in previous researches (Kaya and Tuncer, 2006; 2008a; Soueid *et al.*, 2009) only the extreme point is given. This point is not sufficient, however, to exploit the MAV in all operational situations.

Table 5 Plunging airfoil performances at the characteristic points for $Re = 3.3 \times 10^3$

Point	k	h_0	S_t	η_{app} (%)	η_{sim} (%)	ξ (%)	C_t	C_p
SP	2.707	0.210	0.181	21.3	21.0	1.7	0.112	0.533
NP	2.707	0.270	0.233	21.4	21.1	1.4	0.213	1.011
WP	2.507	0.245	0.195	21.2	21.5	1.3	0.137	0.635
EP	2.907	0.245	0.227	21.3	21.3	0.3	0.206	0.969

Table 6 Plunging airfoil performances at the characteristic points for $Re = 1.1 \times 10^4$

Point	k	h_0	S_t	η_{app} (%)	η_{sim} (%)	ξ (%)	C_t	C_p
SP	2.356	0.185	0.139	27.7	27.8	0.4	0.077	0.276
NP	2.357	0.225	0.169	27.8	27.5	0.8	0.121	0.439
WP	2.157	0.205	0.141	27.6	27.3	1.2	0.077	0.282
EP	2.807	0.205	0.183	27.7	27.3	1.7	0.153	0.561

Table 7 Plunging airfoil performances at the characteristic points for $Re = 2.2 \times 10^4$

Point	k	h_0	S_t	η_{app} (%)	η_{sim} (%)	ξ (%)	C_t	C_p
SP	2.207	0.155	0.109	30.4	30.2	0.5	0.049	0.160
NP	2.207	0.220	0.155	30.8	30.5	1.2	0.112	0.366
WP	1.957	0.185	0.115	30.8	30.7	0.2	0.055	0.179
EP	2.707	0.185	0.159	30.8	30.6	0.6	0.124	0.406

6 Conclusions

An RSM-based optimization technique has been proposed to improve the kinematics of a plunging NACA0012 airfoil. The laminar flow field around the airfoil has been solved for various Reynolds number values. The propulsive efficiency has been maximized on the basis of two control parameters: the reduced frequency and the amplitude of the plunging motion. The proposed optimization technique, which is based on a progressive reduction of the interest region, has been implemented. This technique uses a Nelder-Mead algorithm based search over the constructed response surfaces. Good estimations of the maximum efficiency has been obtained. Also, it was found that, whatever the Re value for a given high propulsive efficiency level, large thrust forces are achievable by applying high frequencies, reducing the input power is possible by adopting low plunging amplitudes. As a future work, we intend to extend this study to handle pitching motion, examine the effect of the control parameters on the acoustic signature, and use other optimization techniques. Furthermore,

an experimental setup is under construction to verify the effectiveness of the obtained numerical results.

References

Anderson, J.M., Streitlien, K., Barrett, D.S., Triantafyllou, M.S., 1998. Oscillating foils of high propulsive efficiency. *Journal of Fluid Mechanics*, **360**:41-72.

Bansmer, S., Radespiel, R., Unger, R., Haupt, M., Horst, P., 2010. Experimental and numerical fluid-structure analysis of rigid and flexible flapping airfoils. *AIAA Journal*, **48**(9):1959-1974. [doi:10.2514/1.J050158]

Betz, A., 1912. Ein beitrag zur erklarung des segelfluges. *Zeitschrift fur Flugtechnik und Motorluftschiffahrt*, **3**:269-272 (in German).

Box, G.E.P., Draper, N.R., 2007. Response Surfaces, Mixtures, and Ridge Analyses (2nd Ed.). John Wiley & Sons, Inc., USA.

Dickinson, M.H., Götz, K.G., 1993. Unsteady aerodynamic performance of model wings at low Reynolds numbers. *Journal of Experimental Biology*, **174**:45-64.

Dickinson, M.H., Lehmann, F.O., Sane, S.P., 1999. Wing rotation and the aerodynamic basis of insect flight. *Science*, **284**(5422):1954-1960. [doi:10.1126/science.284.5422.1954]

Ellington, C.P., 1984. The aerodynamics of hovering insect flight. I. The quasi-steady analysis. *Philosophical Transactions of the Royal Society B: Biological Sciences*, **305**(1122):1-15. [doi:10.1098/rstb.1984.0049]

Ellington, C.P., van den Berg, C., Willmott, A., Thomas, A.L.R., 1996. Leading edge vortices in insect flight. *Nature*, **384**:626-630. [doi:10.1038/384626a0]

Garrick, I.E., 1936. Propulsion of a Flapping and Oscillating Airfoil. NACA Technical Report No. 567.

Haftka, R., Scott, E.P., Cruz, J.R., 1998. Optimization and experiments: a survey. *Applied Mechanics Review*, **51**(7):435-448. [doi:10.1115/1.3099014]

Heathcote, S., Wang, Z., Gursul, I., 2008. Effect of spanwise flexibility on flapping wing propulsion. *Journal of Fluids and Structures*, **24**(2):183-199. [doi:10.1016/j.jfluidstructs.2007.08.003]

Isogai, K., Shinmoto, Y., Watanabe, Y., 1999. Effects of dynamic stall on propulsive efficiency and thrust of flapping airfoil. *AIAA Journal*, **37**(10):1145-1151. [doi:10.2514/2.589]

Jones, K.D., Platzer, M.F., 1997. Numerical Computation of Flapping Wing Propulsion and Power Extraction. 35th AIAA Aerospace Sciences Meeting and Exhibit, Reno, Nevada, USA, No. 97-0826.

Jones, K.D., Platzer, M.F., 2001. On the Use of Vortex Flows for the Propulsion of Micro-Air and Sea Vehicles. Applied Vehicle Technology Panel (AVT), Norway, p.40-1-40-13.

Jones, K.D., Dohring, C.M., Platzer, M.F., 1998. An experimental and computational investigation of the Knoller-Betz effect. *AIAA Journal*, **36**(7):1240-1246. [doi:10.2514/2.505]

Katzmayr, R., 1922. Effect of Periodic Changes of Angle of Attack on Behaviour of Airfoils. NACA Technical Report No. TM 147.

Kaya, M., Tuncer, I.H., 2006. Path Optimization of Flapping Airfoils Based on NURBS. Proceedings of International Conference on Parallel Computational Fluid Dynamics, Busan, Korea.

Kaya, M., Tuncer, I.H., 2008a. Path Optimization of Dual Airfoils Flapping in a Biplane Configuration Using Response Surface Methodology in a Parallel Computing Environment. Proceedings of International Conference on Parallel Computational Fluid Dynamics, Lyon, France.

Kaya, M., Tuncer, I.H., 2008b. Path Optimization of Thrust Producing Flapping Airfoils Using Response Surface Methodology. 5th European Congress on Computational Methods in Applied Sciences and Engendering, Venice, Italy.

Knoller, R., 1909. Die gesetze des luftwiderstands. *Flug-und Motortechnik*, **3**:1-7 (in German).

Lai, J.C.S., Platzer, M.F., 1999. Jet characteristics of a plunging airfoil. *AIAA Journal*, **37**(12):1529-1537. [doi:10.2514/2.641]

Lian, Y., Shyy, W., 2007. Aerodynamics of Low Reynolds Number Plunging Airfoil Under Gusty Environment. 45th AIAA Aerospace Sciences Meeting and Exhibit, Reno, Nevada, USA, AIAA-2007-71.

Miao, J.M., Ho, M.H, 2006. Effect of flexure on aerodynamic propulsive efficiency of flapping flexible airfoil. *Journal of Fluids and Structures*, **22**(3):401-419. [doi:10.1016/j.jfluidstructs.2005.11.004]

Münch, C., Ausoni, P., Braun, O., Farhat, M., Avellan, F., 2010. Fluid-structure coupling for an oscillating hydrofoil. *Journal of Fluids and Structures*, **26**(7):1018-1033. [doi:10.1016/j.jfluidstructs.2010.07.002]

Platzer, M.F., Jones, K.D., Young, J., Lai, J.C.S., 2008. Flapping-wing aerodynamics: progress and challenges. *AIAA Journal*, **46**(9):2136-2149. [doi:10.2514/1.29263]

Ramamurti, R., Sandberg, W., 2001. Simulation of flow about flapping airfoils using finite element incompressible flow solver. *AIAA Journal*, **39**(2):253-260. [doi:10.2514/2.1320]

Raymer, D.P., 2002. Enhancing Aircraft Conceptual Design Using Multidisciplinary Optimization. PhD Thesis, Royal Institute of Technology, Stockholm, Sweden.

Rodriguez, D.L., 2003. Response Surface Based Optimization with a Cartesian CFD Method. 41st AIAA Aerospace Sciences Meeting, Reno, Nevada, USA, AIAA-2003-0465.

Sane, S.P., 2003. The aerodynamics of insect flight. *Journal of Experimental Biology*, **206**:4191-4208. [doi:10.1242/jeb.00663]

Schouveiler, L., Hover, F.S., Triantafyllou, M.S., 2005. Performance of flapping foil propulsion. *Journal of Fluids and Structures*, **20**(7):949-959. [doi:10.1016/j.jfluidstructs.2005.05.009]

Shyy, W., Berg, M., Ljungqvist, D., 1999. Flapping and flexible wings for biological and micro air vehicles. *Progress in Aerospace Sciences*, **35**(5):455-505. [doi:10.1016/S0376-0421(98)00016-5]

Soueid, H., Guglielmini, L., Airiau, C., Bottaro, A., 2009. Optimization of the motion of a flapping airfoil using sensitivity functions. *Computers & Fluids*, **38**(4):861-874. [doi:10.1016/j.compfluid.2008.09.012]

Theodorsen, T., 1935. General Theory of Aerodynamic Instability and the Mechanism of Flutter. NASA Technical Report No. 496.

Tuncer, I.H., Platzer, M.F., 2000. Computational study of flapping airfoil aerodynamics. *AIAA Journal of Aircraft*, **37**(3):514-520. [doi:10.2514/2.2628]

Tuncer, I.H., Kaya, M., 2005. Optimization of flapping airfoils for maximum thrust and propulsive efficiency. *AIAA Journal*, **43**(11):2329-2336. [doi:10.2514/1.816]

Wang, G.G., Dong, Z., 2000. Design optimization of a complex mechanical system using adaptive response surface method. *Transactions of the CSME*, **24**(1B):295-306.

Yang, W.Y., Cao, W., Chung, T.S., Morris, J., 2005. Applied Numerical Methods Using Matlab. John Wiley & Sons Inc., USA.

Yang, S., Luo, S., Liu, F., Tsai, H.M., 2006. Optimization of Unstalled Pitching and Plunging Motion of an Airfoil. 44th AIAA Aerospace Sciences Meeting and Exhibit, Reno, Nevada, USA, No. 06-1055.

Young, J., Lai, J.C.S., 2004. Oscillation frequency and amplitude effects on the wake of a plunging airfoil. *AIAA Journal*, **42**(10):2042-2052. [doi:10.2514/1.5070]

Young, J., Lai, J.C.S., 2007. Mechanisms influencing the efficiency of oscillating airfoil propulsion. *AIAA Journal*, **45**(7):1695-1702. [doi:10.2514/1.27628]